Chapter 1

Fabrication and Sensing Applications of Special Microstructured Optical Fibers

Zhengyong Liu and Hwa-Yaw Tam

Additional information is available at the end of the chapter

http://dx.doi.org/10.5772/intechopen.70755

Abstract

This chapter presents the fabrication of the special microstructured optical fibers (MOFs) and the development of sensing applications based on the fabricated fibers. Particularly, several types of MOFs including birefringent and photosensitive fibers will be introduced. To fabricate the special MOFs, the stack-and-draw technique is employed to introduce asymmetrical stress distribution in the fibers. The microstructure of MOFs includes conventional hexagonal assembles, large-air hole structures, as well as suspended microfibers. The birefringence of MOFs can reach up to 10^{-2} by designing the air hole structure properly. Fiber Bragg gratings as well as Sagnac interferometers are developed based on the fabricated special MOFs to conduct sensing measurement. Various sensing applications based on MOFs are introduced.

Keywords: microstructured optical fibers, MOFs, fiber sensor, interferometry, FBG

1. Introduction

Microstructured optical fibers (MOFs), which have air-hole structure along the fiber length, have attracted tremendous attention in the development of novel fiber sensors for a multitude of industry applications. Majority of the effort has been focused on silica photonic crystal fibers (PCFs), which are composed of many air channels arranged in hexagonal (honeycomb) shape [1–3]. Since Phillip St. Russel proposed the use of silica/air structure to design the fiber and realized all-silica single mode PCF in 1990s [4, 5], significant advances were made in supercontinuum generation [6–8], fiber lasers [9–11], as well as fiber-optic sensor [12–14]. More flexible fiber design and different kinds of materials are used in MOFs, for example, using tellurite or chalcogenide glass rather than pure silica glass [7] and suspended-core structure instead of honeycomb arrangement [13]. Light is guided in PCFs by two principles, namely, the modified total internal

reflection (M-TIR) and the photonic bandgap (PBG). Typically, fibers employing the M-TIR principle have a solid core made of pure silica or silica doped with metal ions (e.g., Ge, Er, Yb, Tm, Co), whereas PCFs using the PBG principle have hollow core. Even though the fiber core is free of dopants or hollow, light can be confined in the core by cladding with periodic air-hole structure due to the lower effective refractive index of cladding or the bandgap effect. The air-hole structure or dopants of MOFs modified the mechanical and optical properties of the fibers, and thus, the MOFs can be tailored to suit specific sensor requirements.

Physical parameters, such as strain, temperature, pressure, vibration, torsion, etc., have been measured accurately using PCF-based sensors [15, 16]. Basically, the air-hole structure in MOFs for sensing applications is designed to give the desired stress distribution in the fiber so that the stress is enhanced by any external physical perturbation to the fiber, leading to change of the effective index of the guided mode in the core. The stress change can be induced either thermally or mechanically such as pulling, compression, and twist. Various kinds of sensors can be implemented using such approach. For instance, polarization-maintaining PCFs with an asymmetrical stress distribution provide an excellent option to construct Sagnac interferometer for the measurement of oil pressure with very high sensitivity of 3.4 nm/MPa [17]. On the other hand, the core in hollow-core PCFs can be filled with gas or analytes to enhance the interaction between the materials in the hollow core and light to realize highly sensitive gas and chemical sensors [18–20]. Alternatively, the air channels in the cladding of index-guiding PCFs confining light via the M-TIR principle can be filled with the materials to be sensed. The materials in the air holes change the index or stress distribution in the cladding and modify the guided light in the core [21–23]. By selectively filling liquid into some of the air holes, refractive index sensor with extremely high sensitivity = 12,750 nm/RIU was reported [23]. The ease and flexibility of fabricating MOFs with different structures bring tremendous opportunities in the development of fiber-optic sensors suited for a wide range of applications.

In this chapter, we present the fabrication techniques of some special MOFs and demonstrate the sensing applications based on the fabricated fibers. The stack-and-draw approach is used to make the fibers; however, specific modifications were introduced to obtain different air-hole structures, especially to induce the asymmetrical stress distribution in the fiber to realize highly sensitive pressure sensors. Various kinds of MOFs including twin-core PCF, high birefringence PCF, suspended core fiber, suspended microfiber, as well as two semicircle holes fiber were fabricated for sensing applications. MOF-based pressure sensors were fabricated using fiber Bragg grating (FBG) and/or interferometry technique. Section 2 will present the fabrication techniques used to fabricate our special MOFs. Section 3 describes the use of MOF sensors for the oil and gas industry. The summary is given at the end of this chapter.

2. Fabrication and characterization of special microstructured optical fibers

2.1. Fabrication of MOFs

Several approaches are being used to fabricate MOFs, including extrusion [24], casting/molding [25], mechanical drilling [26], and stack-and-draw [27]. The stack-and-draw technique is

the most versatile and flexible. This is because by stacking small capillaries, not only various structures can be implemented but also different materials besides silica glass can be utilized. Extrusion, casting, and drilling are widely used to make polymer or soft-glass MOFs due to the much lower softening temperature of these materials. In contrast, it is easier to stack different structures regardless of materials. In addition to fabricate conventional hexagonal air-hole structures, more complicated superlattice structures can be fabricated using circular capillaries that are arranged in patterns to approximate triangular holes, square holes, and elliptic holes [27, 28]. We demonstrated the fabrication of superlattice PCFs using the stack-and-draw technique [27] to realize elliptical holes in the cladding and its optical characteristics are comparable to the design with ideal elliptical holes. Various designs of MOFs with either side hole, two core, or suspended core were used to fabricate optical fiber sensors for different sensing applications. Some of the circular capillaries arranged in hexagonal pattern can be replaced by capillaries/rods of different diameters. The stack-and-draw method offers the flexibility to fabricate a large variety of MOF sensors suited for different industries.

Figure 1 illustrates the process of fabricating a twin-core PCF (TC-PCF) using the stack-and-draw technique. Hexagonal structure is the natural pattern when stacking circular capillaries of equal diameter together. Typically, pure silica capillaries and rods are first drawn before the stacking process. To fabricate PCFs with n-layer of air hole in hexagonal pattern, $3\,n\,(n+1)$ of capillaries plus one rod for the central core are required. The stacked assemble can be secured using tungsten wire and then fixed in position by melting some of the capillaries. Alternatively, the entire assemble can be directly stacked inside a jacket tube, and the gaps are filled with silica rods of various outer diameters.

Basically, two drawing stages are employed to fabricate MOFs, particularly for complicated structures that have many layers of air holes. The first drawing stage is to draw the stacked assembly into cane with the desired outer diameter of 1–2 mm, as illustrated in **Figure 1(c)**. The

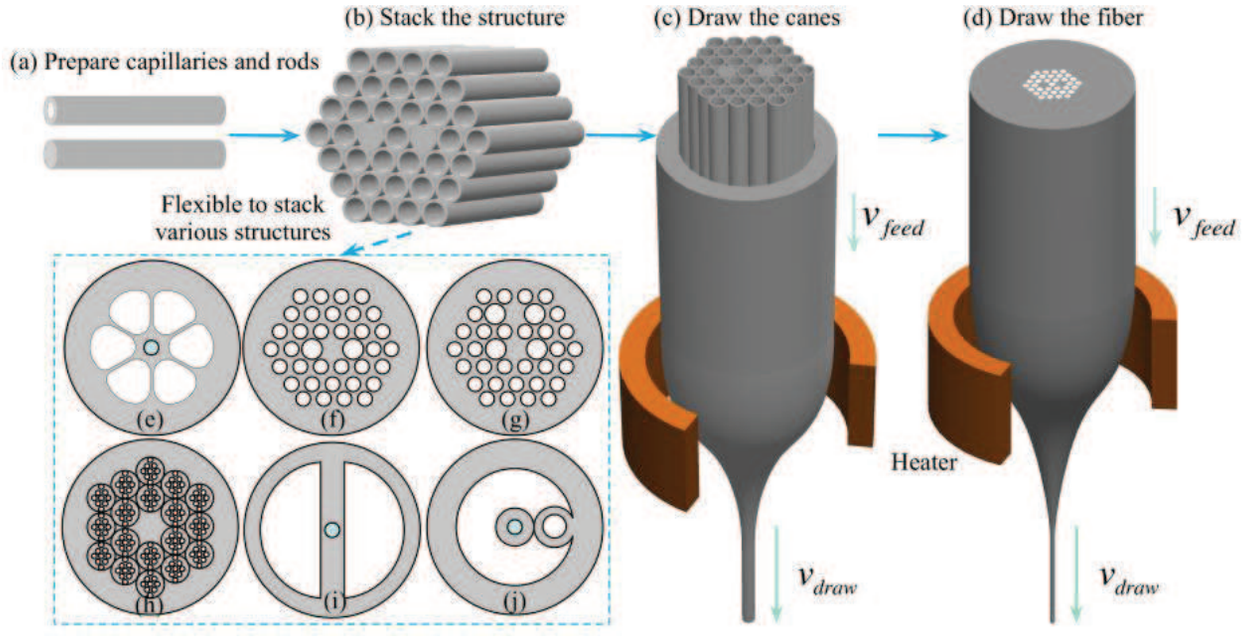

Figure 1. Illustration of the stack-and-draw method used in microstructured optical fibers (MOFs) fabrication.

cane is then inserted into a jacket tube, forming a second preform. The final fiber is drawn from the second preform, as shown in **Figure 1(d)**. By using two drawing stages, the total reduction ratio of diameter can be divided into two parts. Using smaller reduction ratio during the first drawing stage, the stacked assemble can be drawn with minimal distortion from the desired structure. For simple structures or structures with only a few large air holes, one drawing stage is normally adequate. For the superlattice structure reported in Ref. [27], three drawing stages were used, where the first drawn cane was used to make a second stack. To draw the MOFs properly, the drawing temperature ≈ 1900°C is lower than that of pulling all silica single mode fiber (SMF). The air hole would collapse if the drawing temperature is too high [29]. The collapse ratio is inversely proportional to the viscosity and the ratio of drawing velocity over feeding velocity (i.e., $v_{\text{draw}}/v_{\text{feed}}$). High temperature leads to low viscosity and ultimately large collapse ratio. Collapse ratio equal to 1 means air holes completely collapse. Relatively fast drawing velocity is preferable to maintain a certain tension to sustain the air-hole structure. However, large tension also results in poor fiber strength, which makes the fiber fragile. Thus, there is a trade-off to adjust the drawing temperature and tension. The control of tension and temperature is particularly important for drawing MOFs with large air holes.

Figure 2 shows the scanning electronic microscopic (SEM) photos of the cross-section of some fabricated MOFs in our lab using the stack-and-draw technique. By introducing air holes with different diameters, the mechanical properties of the fiber can be modified. In particular, the noncircularly symmetrical air-hole structure provides some degree of tailoring the stress

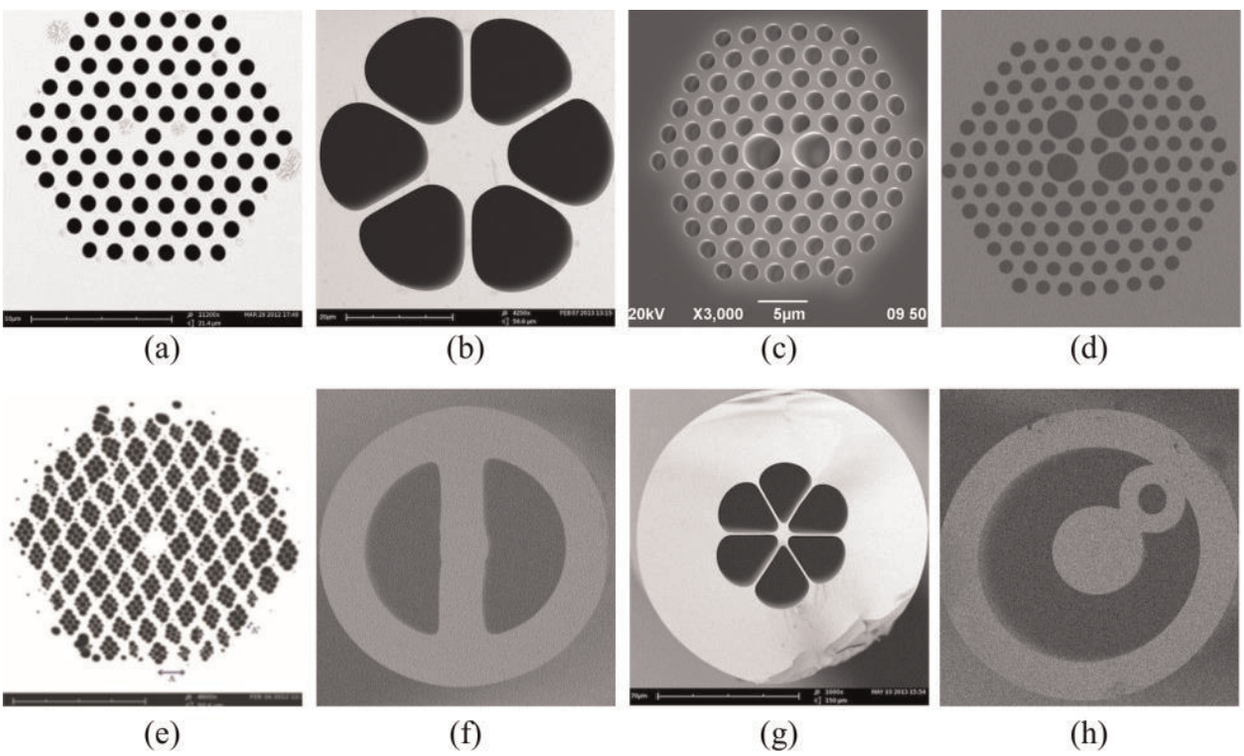

Figure 2. Scanning electronic microscopic photos of the cross section of the fabricated MOFs by using various stacking strategies. The examples shown are (a) twin-core photonic crystal fiber (TC-PCF) [12], (b) six-hole suspended-core fiber (SH-SCF), (c) high birefringence PCF (HB-PCF), (d) two-core HB-PCF, (e) superlattice PCF [27], (f) two semicircle hole fiber, (g) high birefringence suspended-core fiber (HB-SCF) [13], and (h) single-ring suspended fiber [30].

distribution in the fiber. Basically, the stress distribution of circularly symmetrical structures, including the standard single-mode optical fiber, is identical along the two polarization axes. MOFs with noncircularly symmetrical cross-section are birefringent. **Figure 2(a)** shows a two-core MOF, where the optical coupling between the cores is affected by pressure. **Figure 2(b)** shows a 6-hole MOF for the measurement of refractive-index changes of fluid. The cores of the MOFs shown in **Figure 2(c)–(g)** are elliptical, and the fibers are highly birefringent. **Figure 2(h)** shows a small-diameter fiber suspended inside a fiber and is designed for vibration measurement.

2.2. Twin-core photonic crystal fiber

A twin-core PCF was developed as an alternative sensor to standard single-mode optical fiber for pressure measurement. The air-hole structure of the TC-PCF is shown in **Figure 2(a)**, where two capillaries are replaced by two pure silica rods in the stacked assembly. The fabrication process is described schematically in **Figure 1**, and details can be found in Ref. [12]. The fiber was drawn at a temperature close to 1900 C. The outer diameter of the fiber is 125 μm, and diameter of two cores is ~2.5 μm. The hole diameter is ~1.1 μm, and pitch is ~1.85 μm. As the distance between the two cores is so close (~4 μm), the coupling effect between each other is strong. The modes guided in each core are combined and known as supermodes, i.e., even and odd modes [12, 31, 32]. Particularly in the fabricated TC-PCF, there are *x*-polarized even and odd modes and *y*-polarized even and odd modes. **Figure 3** shows the simulated mode profile of these modes.

According to the coupling theory, the coupling length of even and odd modes at each polarization (e.g. *x* polarization) can be written as

$$L_c(\lambda) = \frac{\lambda}{2\left|n_{p,x-even} - n_{p,x-odd}\right|} = \frac{\lambda}{2\left|\Delta n_{x,p}\right|}, \tag{1}$$

where $n_{p,x\text{-}even}$ and $n_{p,x\text{-}odd}$ represent the phase effective index of the x-polarized even and odd modes respectively, and $\Delta n_{p,x}$ stands for their difference. The effective index of each mode changes with the stress distribution induced by the external environment (such as pressure and strain), which eventually causes the corresponding change of coupling coefficient. As for

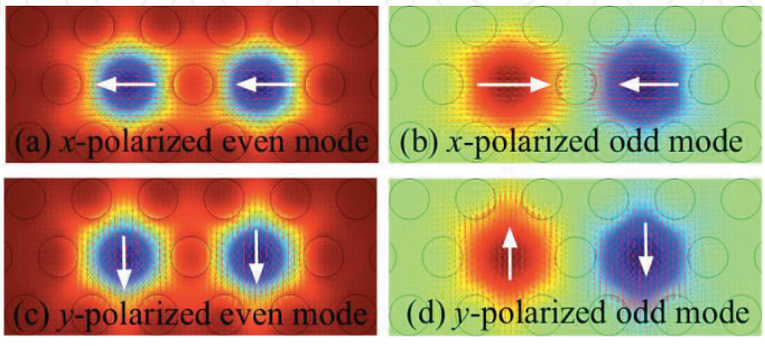

Figure 3. Simulated profiles of the electrical field for the *x*-polarized even and odd modes and *y*-polarized even and odd modes supported in TC-PCF, where the arrows show the direction of the field (adapted from ref. [12], OSA).

one polarization direction, the power coupled from one core to the other after propagating a distance of L can be expressed as

$$I_x(\lambda) = \sin^2\left[\frac{\pi}{2L_c(\lambda)}L\right] = \sin^2\left(\frac{\pi}{\lambda}\Delta n_{x,p}L\right). \tag{2}$$

Since the x and y polarization are orthogonal, the total output power of the transmission is the sum of both polarizations, which is then expressed as

$$I(\lambda) = I_x(\lambda) + I_y(\lambda) = 1 - \cos\left[\frac{\pi}{\lambda}\left(\Delta n_{x,p} + \Delta n_{y,p}\right)L\right] \cdot \cos\left[\frac{\pi}{\lambda}\left(\Delta n_{x,p} - \Delta n_{y,p}\right)L\right]. \tag{3}$$

It can be seen that the transmission spectrum of the TC-PCF is modulated due to the mutual influence of the two polarizations. If considering a short wavelength range, the fringe spacing can be approximated as

$$\Delta\lambda = \frac{2\lambda^2}{\left(\Delta n_{x,g} + \Delta n_{y,g}\right)L}. \tag{4}$$

Here, $\Delta n_{x,g}$ and $\Delta n_{y,g}$ are the group effective index difference of the even and odd modes of x- and y-polarizations, respectively. The group index (n_g) and phase index (n_p) have a relationship of $n_g = n_p - \lambda dn_p/d\lambda$. The calculated $\Delta n_{x,g}$ and $\Delta n_{y,g}$ are 3.745×10^{-3} and 3.386×10^{-3}, respectively. The calculated fringe spacing for a 110-cm long TC-PCF is ~0.613 nm. In experiment, the TC-PCF was spliced to two SMFs using manual splicing mode [33, 34]. A broadband source (BBS) and optical spectrum analyzer (OSA) were utilized to monitor the transmission spectrum of the output. To obtain high fringe contrast, an offset in the alignment and repeated arc discharges are needed. **Figure 4** shows the calculated and experimental transmission spectrum. Both results show modulation on the interference. Besides, the fringe spacing obtained experimentally is about 0.676 nm, which is also in good agreement with the calculated value. The obtained transmission spectrum of TC-PCF is sensitive to external physical perturbation and can be employed as pressure sensors.

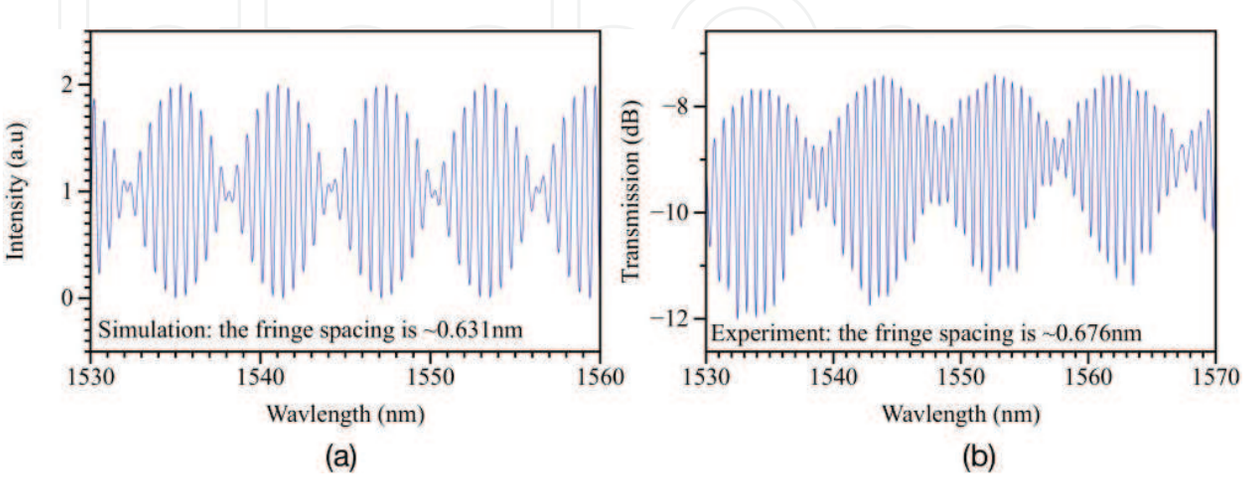

Figure 4. (a) Simulated and (b) experimental transmission spectra of a 110-cm long TC-PCF, adapted from ref. [12], OSA.

2.3. High birefringence microstructured optical fiber

In addition to the multiple cores achieved by replacing certain capillaries during stacking, capillaries with different inner diameters can be used to fabricate noncircularly symmetric air-hole structures to introduce birefringence in MOFs. The effective index of the *x*-polarized mode and *y*-polarized mode is different in birefringent MOFs. The birefringence of the fiber is defined as the index difference of the two polarization modes (i.e., $B = |n_x - n_y|$). In optical fiber communications, birefringent fiber is utilized to realize polarization maintaining. Commonly used polarization-maintaining fibers (PMFs) have a bowtie, elliptical, or PANDA structures [35]. The main feature of these fibers is that there are two heavily doped parts in the cladding, e.g., *PANDA* fiber [36] or an elliptical core designed to induce noncircularly symmetric stress to the core. The stress applying part in the cladding or the asymmetrical geometry of the fiber is regarded as exterior stress to the fiber core, whereas the thermal expansion of the noncircularly symmetric core yields interior stress to the core. The total birefringence of the fiber is composed of the contributions from exterior stress, interior stress, or both, depending on the fiber type.

Similar concept is employed in MOFs. Unlike conventional PMFs, high birefringence MOFs (HB-MOFs) exhibit the flexibility of modifying the fiber geometry and inducing exterior stress to the core. MOF fabrication permits the ease of introducing various air-hole structures in the cladding and breaks the circular symmetry of the fiber. Birefringence is an important property in fiber sensors for the measurement of many physical parameters. PM-PCF has been demonstrated to be a good candidate in the measurements of pressure [17], strain [37], temperature [38], torsion [39], etc. Most of these applications are based on the commercially available PM-PCF from NKT Photonics (PM-1550-01), which has a birefringence of ~4×10^{-4} at the wavelength of ~1550 nm.

The birefringence of MOFs allows for the construction of Sagnac interferometer (SI) by simply splicing PM-PCF between two output ports of a 3-dB coupler. The 3-dB coupler splits the light from one input port into two counter-propagating beams that interfere with each other at the 3-dB coupler after propagating through the PM-PCF, as shown in **Figure 5(a)**. The phase difference (ϕ) of the two polarization is $2\pi BL/\lambda$, where B and L are the birefringence and length of the fiber, respectively. At the valleys of the spectrum, the phase difference is always equal to $2k\pi$ (k is an integer). As for two adjacent valleys, the change of phase difference is 2π and equals $(d\phi/d\lambda)^*\Delta\lambda$, where $\Delta\lambda$ is the wavelength difference of these two adjacent valleys. Thus, the birefringence of one HB-MOF can be expressed by

$$G = \frac{\lambda_1 \cdot \lambda_2}{\Delta\lambda \cdot L}, \tag{5}$$

where λ_1 and λ_2 represents the two adjacent valley wavelengths and G is the group birefringence, which can be measured via the experimental SI spectrum. **Figure 5(b)** plots the spectrum of a typical SI constructed using in-house HB-PCF (shown in **Figure 2(c)**) having a length of 5.5 cm. The wavelengths of two valleys close to 1550 nm are 1547.16 nm and 1550.66 nm. The group birefringence of this fiber is calculated to be ~1.25×10^{-2}.

The birefringence of the MOFs offers an alternative to conventional PMFs in the construction of interferometric sensors using phase difference of two polarization modes propagating in the

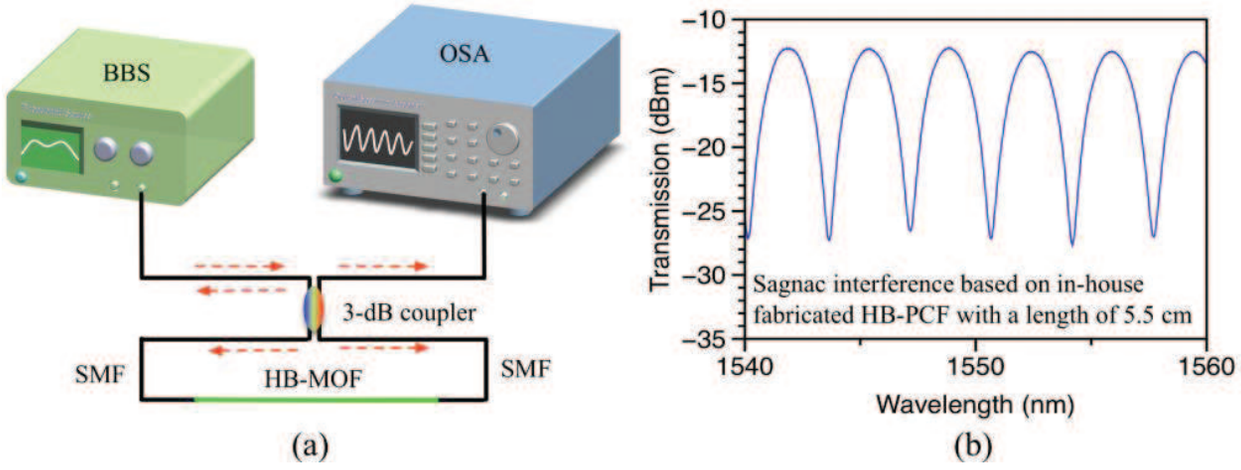

Figure 5. (a) Schematic figure of the configuration of a typical Sagnac interferometer realized by HB-MOF and (b) interference spectrum of a SI based on a 5.5-cm long in-house fabricated HB-PCF.

MOFs. The sensitivity of interferometric sensors is highly dependent on the birefringence change induced by external perturbations. Therefore, the arrangement of the air-hole structure that transfers the external perturbation to the optical mode in the core is important. We designed and fabricated several types of MOFs to measure oil pressure and refractive index of fluid for biomedical sensing. The sensitivity of the sensors varies greatly with the geometry of the core and cladding, as well as the sensing principle employed in the sensors. In general, interferometry-based sensors exhibit better sensitivity than grating-based sensors. However, in interferometry-based sensors, the sensing information is encoded in the spectral dips/peaks, which is much broader than the reflection peaks of grating-based sensors. Detecting the shift of the dips/peaks of a broad spectrum accurately is more difficult, therefore could affect the measurement accuracy. The sensing performance of different MOFs will be presented and compared in the following two sections.

Figure 2(c)–(g) show the SEM photos of some of the MOFs with high birefringence fabricated in our lab. As the air-hole structure is different, the birefringence of the fibers is not the same. The phase and group birefringence of HB-PCF we fabricated (show in **Figure 2(c)**) are measured to be 1.1×10^{-2} and 1.25×10^{-2}. Both values are in good agreement with the calculated values of 1.4×10^{-2} using finite element method. The two large holes in the cross section of the fiber shown in **Figure 2(c)** are slightly elongated, resulting in the desired noncircularly symmetric air-hole structure for high birefringent fiber. For index-guiding MOFs made of silica, this fiber possesses the highest birefringence in reported literatures. **Table 1** lists the comparison of our various HB-MOFs and others reported in the literatures.

Basically, elliptical core leads to higher birefringence because the two polarization modes are along with the major and minor axis of the elliptical core, individually. Due to the feature that optical mode is confined in the air for hollow-core PCF, even slight imperfection can influence the light propagation significantly, such as the loss and modal profile. Thus, hollow-core PCF with elliptical core exhibits very high birefringence even for small ellipticity. For example, the elliptical core with an aspect ratio of 1.16 exhibits a group birefringence of 2.5×10^{-2} [52]. MOFs

PM fiber type	Description of the structure	Reported date	Measured birefringence
HB PM-PCF, **Figure 2(c)**	Two large holes close to an elliptical core	May, 2013 [40]	1.25×10^{-2}
Superlattice PCF, **Figure 2(e)**	Superlattice with rhombic cell of 9 holes	June, 2014 [27]	8.5×10^{-4}
6-hole suspended-core fiber, **Figure 2(g)**	Elliptical core suspended by 6 large air holes	June, 2014 [13]	5×10^{-4}
Semicircle hole fiber, **Figure 2(f)**	Two large semicircle side holes	August, 2017	1×10^{-4}
Low-loss PM-PCF	Two large air holes close to the core	December, 2011 [41]	1.4×10^{-3}
PANDA PMF	Stress-applying parts with PANDA shape	July, 1981 [42]	8.5×10^{-5}
Bow-tie PMF	Stress-applying parts with bow-tie shape	November, 1982 [43]	4.87×10^{-4}
First fabricated HB PCF	Twofold rotational symmetry	September, 2000 [44]	3.85×10^{-3}
Side-hole fiber	Two side holes with elliptical Ge-core	September, 2008 [45]	1.39×10^{-4}
HB MOF	Irregular air holes with elliptical core	July, 2007 [46]	1.1×10^{-2}
Butterfly-type MOF	Twofold air-hole structure with butterfly shape	June, 2010 [47]	1.8×10^{-3}
Squeezed lattice PCF	Squeezed air holes with two big holes	February, 2010 [48]	5.5×10^{-3}
HB index-guiding PCF	Elliptical core by achieved by replacing two holes	June, 2001 [49]	9.3×10^{-4}
Fiberized glass ridge waveguide	Borosilicate glass-based fiberized ridge waveguide	April, 2015 [50]	9.5×10^{-3}
HB nonlinear MOF	Small elliptical core	July, 2004 [51]	7×10^{-3}
Hollow-core PBGF	Elliptical hollow core	August, 2004 [52]	2.5×10^{-2}
SF57 glass MOF at 1.06 μm wavelength	Asymmetric structure with elliptical air holes	May, 2017 [53]	9×10^{-2}
Chalcogenide glass PCF at 7.5 μm wavelength	Two large air holes close to the core	April, 2016 [54]	1.5×10^{-3}

Table 1. Comparison of birefringent MOFs reported in the literatures.

made of other type of glass (e.g. SF57, Chalcogenide glass) also have large birefringence in the order of 10^{-2}, if the structure is optimized. Sensors with high birefringence allow the implementation of compact sensing configuration because shorter fiber can be used. The sensing information of Sagnac interferometer is encoded in the wavelength shift of the interference spectrum. The phase difference at one valley is equal to $2k\pi$, and the sensitivity, which is defined as the wavelength shift per unit change in the measurand, can be expressed by

$$\frac{d\lambda}{dX} = \frac{\lambda}{G}\frac{\partial B}{\partial X}, \tag{6}$$

where X is the measurand, such as pressure, temperature, refractive index, etc., B is the modal (phase) birefringence, and $\frac{\partial B}{\partial X}$ is the polarimetric sensitivity. Note that the length effect is neglected in Eq. (6), which is not applied to the strain measurement. The strain is mainly

caused by elongation and thus needs to be taken into account to estimate the sensitivity, which can be formulated by considering the length, and the equation becomes

$$\frac{d\lambda}{d\varepsilon} = \frac{\lambda \cdot [\partial B_1(\lambda, \varepsilon)/\partial\varepsilon + B_1(\lambda, \varepsilon)]}{G_1(\lambda, \varepsilon) + (1/\alpha - 1) \cdot G_2(\lambda)}, \tag{7}$$

where $B_1(\lambda,\varepsilon)$ and $G_1(\lambda,\varepsilon)$ are the phase and group modal birefringence for the MOF section under stressed, $G_2(\lambda)$ is the group modal birefringence for the MOF section without strain applied, and α is the ratio of fiber section under strain over total length of the MOF. Different air-hole structures give different values of birefringence derivative with respect to the measurands; therefore, it is important to design the MOFs with the desirable birefringence derivative to optimize the sensing performance. In terms of the form of wavelength shift, the sensitivity is inversely proportional to the birefringence. The key consideration to achieve high sensitivity is to have large-phase birefringence change with measurands but relatively low-group birefringence.

2.4. Sensors based on fiber Bragg grating inscribed in MOFs

The ease and flexibility of fabrication of birefringent MOFs result in the increasing use of these fibers in Sagnac interferometric sensors. Fiber Bragg gratings can be inscribed in MOFs to increase their sensing capabilities. However, it is more difficult to inscribe FBGs in the MOFs compare to SMFs due to the existence of the air holes that diffract the UV light needed to write gratings. UV light at 193, 248, 213, and 266 nm, as well as femtosecond laser [55–57], is being used to inscribe FBGs in various types of MOFs. 193 nm lasers [56] and femtosecond lasers were used to write FBGs in nonphotosensitive MOFs. These lasers induced physical deformation in the fiber cores. FBG written on MOFs using femtosecond laser can be used for high temperature measurement up to 800°C [56]. There are two reflective peaks instead of one peak in the reflection spectrum of an FBG inscribed in birefringent fibers [40, 58, 59]. The separation of these two peaks is directly related to the fiber birefringence.

It is easy to introduce photosensitivity in MOFs by using a germanium-doped rod during the stacking stage. Gratings can be inscribed in MOFs using UV light, and the ease of grating inscription depends on the air-hole patterns. **Figure 6** shows the reflection spectrum of an FBG inscribed in a six-hole suspended-core fiber (SCF) and HB PCF fabricated in our lab. The SEMs of their cross-section are shown in the insets. By optimizing the inscription system, very strong FBGs can be achieved. Owing to the ultrahigh-phase birefringence (~1.1×10^{-2}), the two reflective peaks of FBG inscribed in HB PCF show very large wavelength separation of more than 10 nm which is much larger than that in the commercial PM-PCF (0.5 nm) [59] and the HB MOFs (2.1 nm) reported in Ref. [58]. Two peaks with large separation allow for simultaneous measurement of temperature and pressure because the stress transferred to the core along the two polarization axes is different when subjected to pressure.

The FBG inscribed in the six-hole suspended-core fiber can be employed to measure strain and temperature. The measured strain sensitivity is about 0.96 pm/μm, which is close to that of SMF. Since the germanium is doped in the core as in SMF, similar temperature sensitivity of

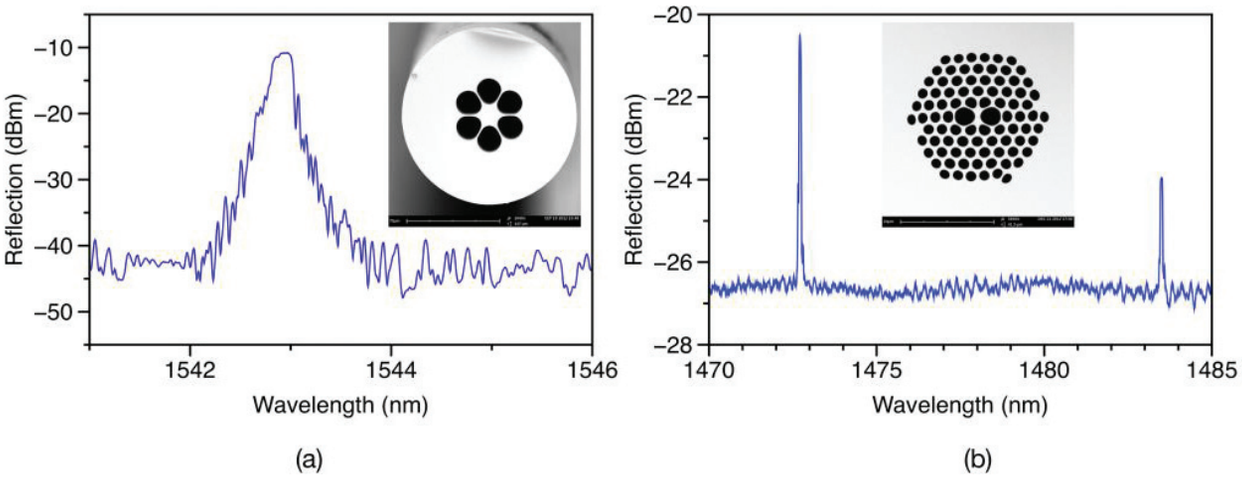

Figure 6. Reflection spectrum of an FBG inscribed in the (a) photosensitive six-hole SCF and (b) HB PCF, adapted from ref. [40], OSA. The insets show the SEM photos of the cross section of the fabricated fibers.

10.7°C was measured. However, the pressure sensitivity of the FBG inscribed in the fiber was measured to be 8.2 pm/MPa, which is higher than that of SMFs, which is ~3.1 pm/MPa [60]. This improvement is due to the six air holes, and further increase in the sensitivity is possible by using larger air holes, as demonstrated in [61]. We designed and fabricated a single-ring suspended fiber, as shown in **Figure 2(h)**, to increase the pressure sensitivity. The measured pressure sensitivity using FBG on this fiber is about 18 pm/MPa, more than 5 times higher than that of standard SMFs.

In addition, the large air holes of MOFs permit materials to be filled in the cladding to functionalize MOFs into a large variety of sensors. For example, low-temperature melting point metal was filled into the air holes of the six-hole SCF to function as anemometer to measure wind speed [22]. The metal absorbs energy from light propagating in the six-hole SCF, and the FBG inscribed in the core measures the temperature change. The cooling rate of the metal/FBG is directly related to the wind speed. Due to the large optical absorption of metal, the heating efficiency is very high, i.e., ~7.3°C/mW. Laser power as low as 14 mW is sufficient to heat the metal/FBG up to 100°C. This is more efficient than the heating process using Co^{2+}-doped fiber as we have demonstrated in [62].

3. Sensing applications of MOFs in the oil and gas industry

The demand for fiber optic sensors in the oil/gas industry comes from the harsh downhole conditions and the depth of oil wells which can be as deep as 12 km. The great distance coupled with the high pressure (up to 100 MPa) and temperature (more than 200°C) of oil in downholes restricts the use of conventional sensors. However, the intrinsic features of optical fiber sensors such as long distance transmission, immune to EMI, and high operating temperature make it a promising candidate for the oil industry. The use of multiple FBGs distributed along a single strand of SMF has been employed in oil monitoring. Key parameters like pressure, temperature, and flow speed are widely measured in oil wells [63, 64]. In such

circumstances, high pressure can cause large irretrievable disasters during oil exploitation and oil transportation. Therefore, it is of great importance to measure pressure, and MOFs are potential candidates to enhance the capabilities of optical fiber sensors used in the oil industry.

The stress distribution around the core of MOFs can be tailored via the air-hole pattern to enhance the MOFs' sensitivity to pressure. The application of pressure to MOFs leads to large compression stress in the fiber core where optical light propagates. Good performance in terms of sensitivity, resolution, as well as fast response can be achieved by properly designing the structure of the MOFs.

The basic principle that permits fiber sensors to measure pressure is the photoelastic effect of silica glass. When subjected to pressure, fiber sensors regardless of the use of different operating principles, the silica fiber shows the corresponding dependence on the change in pressure. Particularly, the refractive index of the core/cladding of MOFs varies with applied pressure, which can be expressed as

$$\begin{bmatrix} n_x \\ n_y \\ n_z \end{bmatrix} = n_0 - \begin{bmatrix} C_1 & C_2 & C_2 \\ C_2 & C_1 & C_2 \\ C_2 & C_2 & C_1 \end{bmatrix} \begin{bmatrix} \sigma_x \\ \sigma_y \\ \sigma_z \end{bmatrix}, \tag{8}$$

where n_i is the index component in i_{th} direction ($i = x, y, z$), σ_i represents the corresponding stress component, and n_0 is the silica index without pressure applied. The constants C_1 and C_2 are the stress-optic coefficient for silica glass and have values of 6.5×10^{-13} and 4.2×10^{-12} m^2/N, respectively. The change in refractive index induced by pressure is determined by the above equation. The pressure-induced change in index is taken into account to calculate the guided mode in MOFs. Either FBGs or interferometry is employed to make pressure sensors, and the stress transfer mechanism is similar. However, in terms of the polarimetric approach based on high birefringence MOFs as introduced in Section 2.3, the resultant pressure sensors that employ the index difference of two polarized modes exhibit better sensitivity.

Figure 7 plots the results of oil pressure measurement using FBGs written on conventional SMF and single-ring suspended fiber (shown in **Figure 2(h)**) with various outer diameters. The single-ring suspended fiber differs from SMF because of the large air region in the fiber, resulting in high air-filling ratio (AFR). AFR of SMF can be regarded as 0, as no air holes exist in the fiber. Typically, higher AFR gives better sensitivity [61]. The measured results using FBG on single-ring suspended fiber show a large improvement (five times) of pressure sensitivity compared to that obtained on SMF. Furthermore, by etching the cladding of the fiber, smaller outer diameter of this MOF means higher AFR and consequently further increases the pressure sensitivity from −18 to −21 pm/MPa.

In addition to improvement in sensitivity, MOFs enable simultaneous measurement of pressure and temperature by using FBG inscribed in high birefringence fiber. As shown in **Figure 6(b)**, the two distinct peaks occurred in the reflection spectrum have a wide wavelength separation due to the large fiber birefringence. The separation is more than 10 nm for this MOF, which has a measured birefringence of 1.1×10^{-2}. Two-parameter measurement tends to be easier when

utilizing two peaks with large separation. **Figure 8(a)** shows the pressure responses of the two modes polarized in fast and slow axes, corresponding to the two FBG peaks located at shorter and longer wavelength, which gives sensitivities of −1.9 pm/MPa for the fast axis peak and −5.1 pm/MPa for the slow axis peak [40]. The different pressure responses obtained from the fast and slow axis peaks are due to the asymmetrical air hole structure, which breaks the uniformity of the pressure-induced stress. Therefore, the stress change along the fast axis is

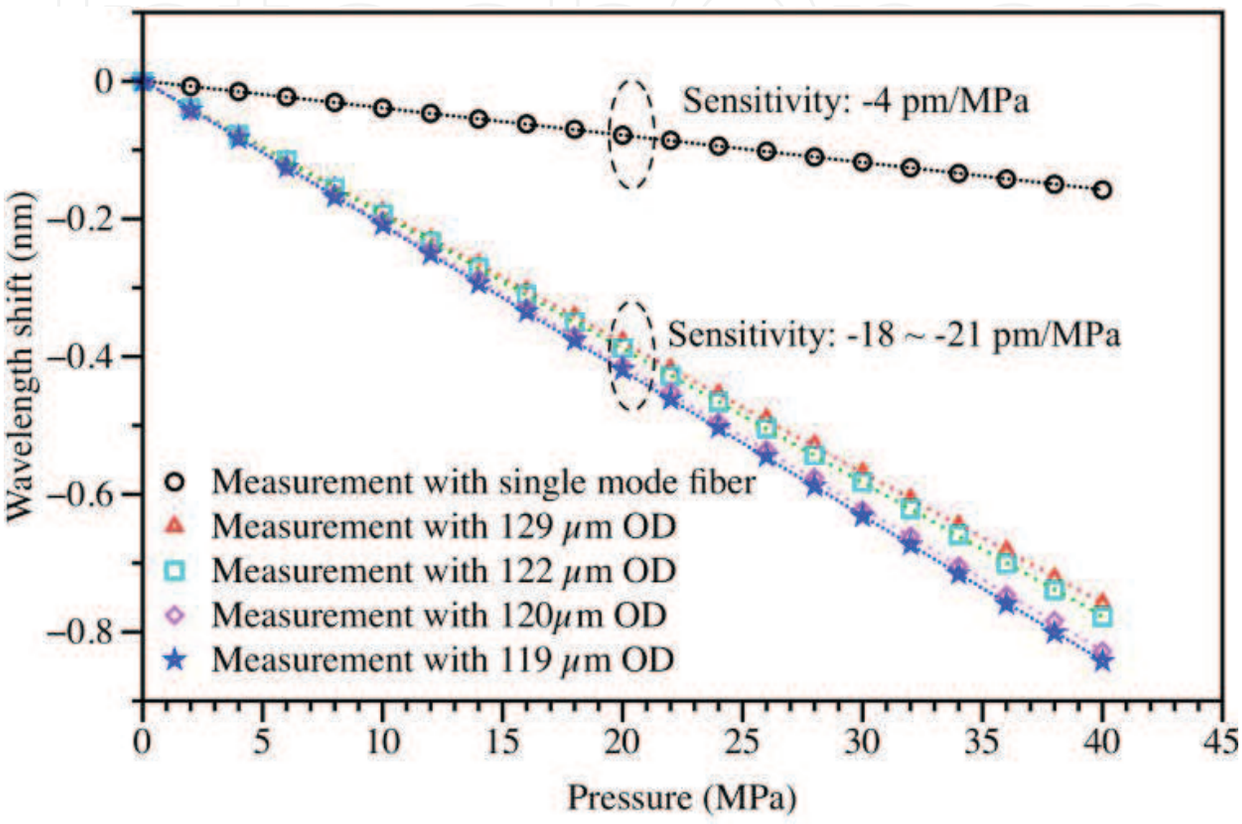

Figure 7. Pressure response of FBGs inscribed in SMF and MOFs.

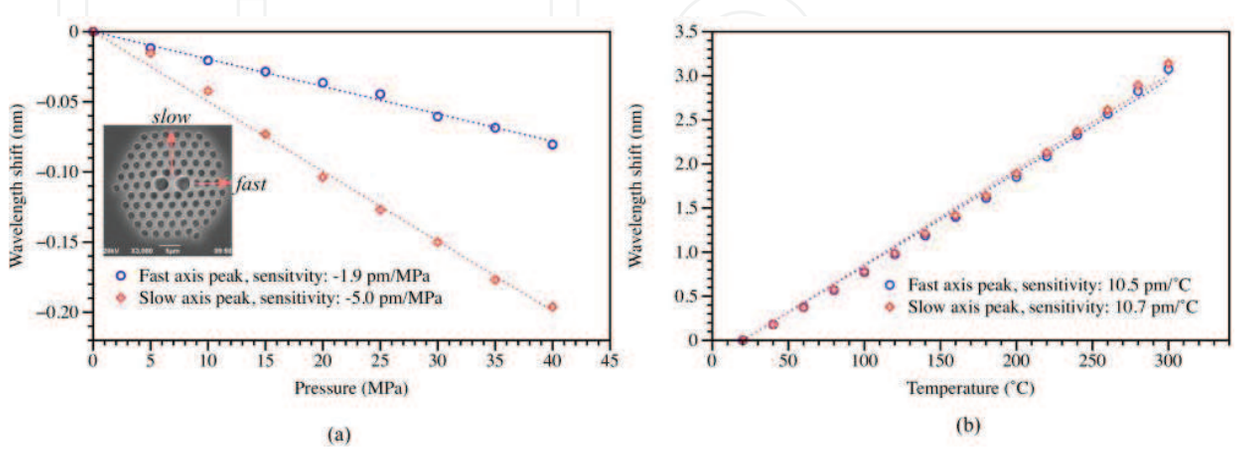

Figure 8. (a) Pressure response of FBG written in the HB-PCF fabricated in our laboratory, where the fast and slow axis peaks show different responses, (b) temperature dependence of the two axes (adapted from Ref. [40], OSA).

smaller than that in the slow axis due to the existence of two large air holes. However, the temperature dependence of the two polarized modes are the same, about 10 pm/°C, as shown in **Figure 8(b)**. Such discrimination in pressure and temperature allows the simultaneous measurement of these two parameters. The change in pressure and temperature can be calculated according to the total wavelength shift of the fast and slow axis grating peak via the following equation

$$\begin{bmatrix} \Delta T \\ \Delta P \end{bmatrix} = \frac{1}{32.17} \begin{bmatrix} -1.9 & 5.0 \\ -10.5 & 10.7 \end{bmatrix} \begin{bmatrix} \Delta\lambda_s \\ \Delta\lambda_f \end{bmatrix}, \tag{9}$$

where $\Delta\lambda_s$ and $\Delta\lambda_f$ are the total wavelength shift for the slow and fast axis grating peaks due to changes in the applied pressure and temperature, respectively.

The pressure sensitivity of FBG sensors is very small, varying from a few to tens of pm/MPa even if special MOFs are employed. The low sensitivity is due to the slight modal index change with respect to pressure. On the other hand, the sensitivity can be improved significantly by applying the polarimetric approaches based on high birefringence MOFs. For example, SI or rocking filter pressure sensors exhibit much higher sensitivity in pressure measurement [65, 66]. The construction of a SI sensor is shown in **Figure 5(a)**, where the MOF is subjected to oil pressure. The oil pressure sensitivity demonstrated by a PM-PCF

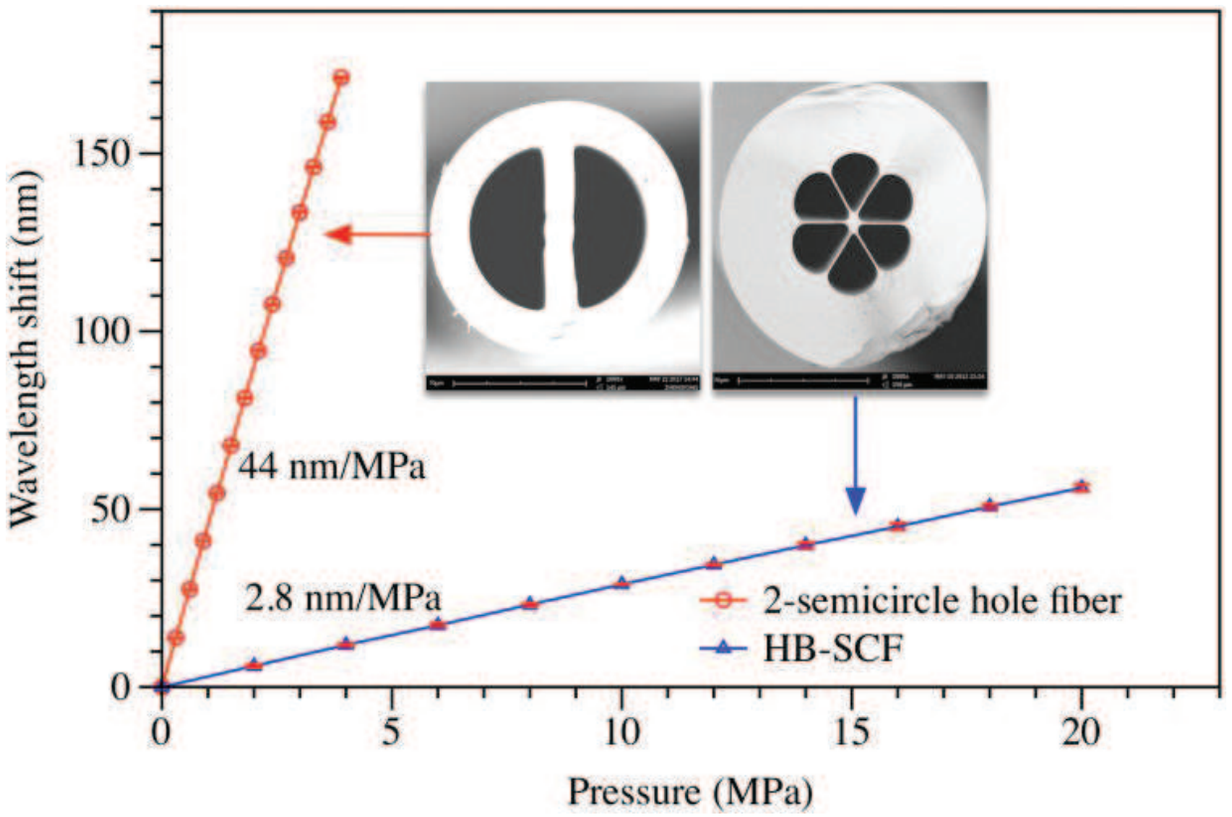

Figure 9. Hydrostatic oil pressure response of Sagnac interferometer realized using HB-SCF [13], (2014 IEEE) and two semicircle hole fiber.

commercially available from NKT Photonics, Inc. is 3.24 nm/MPa at ~1550 nm [67]. The pressure sensitivity of a SI pressure sensor can be written as

$$\frac{d\lambda}{dP} = \frac{\lambda}{G}\frac{dB}{dP}, \tag{10}$$

where the derivative dB/dP represents the phase birefringence change with respect to applied pressure, which means the index difference of two polarized modes is considered rather than only one mode as in the case of FBG sensor. This value can be improved easily by using noncircularly symmetric structure. **Figure 9** shows the wavelength shift as a function of the applied pressure on the highly birefringent MOFs, where (a) plots the results for HB-SCF and (b) is the pressure response for the two semicircle hole fiber. Both measurements are based on SI configuration. The measured pressure sensitivity is ~2.8 nm/MPa using HB-SCF, which is comparable to the commercial PM-PCF. However, the fabrication of HB-SCF is much easier than PM-PCF that has a lot of air holes in honeycomb arrangement [13]. On the other hand, the sensitivity improvement is significant by using the design of two semicircle hole structure, which was measured to be 44 nm/MPa, about 13 times larger than that achieved with commercial PM-PCF. Such great increase owes to the relatively low birefringence (i.e., small G), as well as the cutoff of fast axis by two large semicircle holes (i.e., large dB/dP).

4. Conclusion

To conclude the chapter, several novel structures of optical fibers are proposed and demonstrated for sensing applications. The sensing performance is comparable to and better than most sensors developed based on traditional single-mode fibers (SMFs). The basic fabrication method is briefly reviewed, especially to introduce the asymmetrical stress distribution to MOFs. Due to the novel structure of MOFs, it also exhibits unique feature that SMF does not possess, for instance, the high birefringence. Different air hole structures of MOFs exhibit various mechanical and optical properties that are employed to develop the sensors. The ultrahigh birefringence of HB-PCF can be ~1.2×10^{-2}, which is the highest one for the fabricated index-guiding PCFs. The pressure sensor based on the fabricated two semicircle hole MOF shows very high sensitivity >40 nm/MPa by constructing a Sagnac interferometer. Those sensors can find good applications in oil and gas industry, as well as the biomedical detection. The demonstrated MOFs can give full understanding of developing sensors to measure physical and biomedical parameters, in terms of the design, fabrication of the MOFs, and the approaches to configure sensors.

Acknowledgements

The authors like to acknowledge the financial support by the Hong Kong Polytechnic University under the project of 1-ZVGB.

Author details

Zhengyong Liu* and Hwa-Yaw Tam

*Address all correspondence to: zhengyong.liu@connect.polyu.hk

Photonics Research Centre, Department of Electrical Engineering, The Hong Kong Polytechnic University, Hung Hum, KLN, Hong Kong

References

[1] Knight JC. Photonic crystal fibres. Nature. 2003;**424**:847-851

[2] Russell P. Photonic crystal fibers. Science. 2003;**299**:358-362

[3] Russell PSJ. Photonic-crystal Fibers. Journal of Lightwave Technology. 2006;**24**:4729-4749

[4] Knight J, Birks T, Russell P. All-silica single-mode optical fiber with photonic crystal cladding. Optics Letters. 1996;**21**:1547-1549

[5] Birks TA, Knight JC, Russell PS. Endlessly single-mode photonic crystal fiber. Optics Letters. 1997;**22**:961-963

[6] Dudley JM, Coen S. Supercontinuum generation in photonic crystal fiber. Reviews of Modern Physics. 2006;**78**:1135-1184

[7] Toupin P, Brilland L, Renversez G, Troles J. All-solid all-chalcogenide microstructured optical fiber. Optics Express. 2013;**21**:14643

[8] http://www.nktphotonics.com/lasers-fibers/en/

[9] Kong F, et al. Polarizing ytterbium-doped all-solid photonic bandgap fiber with ~1150μm^2 effective mode area. Optics Express. 2015;**23**:4307

[10] Groothoff N, Canning J, Ryan T, Lyytikainen K, Inglis H. Distributed feedback photonic crystal fibre (DFB-PCF) laser. Optics Express. 2005;**13**:2924-2930

[11] Canning J, et al. All-fibre photonic crystal distributed Bragg reflector (PC-DBR) fibre laser. Optics Express. 2003;**11**:1995-2000

[12] Liu Z, et al. Intermodal coupling of supermodes in a twin-core photonic crystal fiber and its application as a pressure sensor. Optics Express. 2012;**20**:21749-21757

[13] Liu Z, Wu C, Tse M-LV, Tam H-Y. Fabrication, characterization, and sensing applications of a high-birefringence suspended-core fiber. Journal of Lightwave Technology. 2014;**32**: 2113-2122

[14] Monro TM, et al. Sensing with microstructured optical fibres. Measurement Science and Technology. 2001;**12**:854-858

[15] Liu Z, Tam H-Y, Htein L, Tse M-LV, Lu C. Microstructured optical Fiber sensors. Journal of Lightwave Technology. 2017;**35**:3425-3439

[16] Pinto AMR, Lopez-Amo M. Photonic crystal Fibers for sensing applications. Journal of Sensors. 2012;**2012**:1-21

[17] Fu HY, et al. Pressure sensor realized with polarization-maintaining photonic crystal fiber-based Sagnac interferometer. Applied Optics. 2008;**47**:2835-2839

[18] Jin W, Cao Y, Yang F, Ho HL. Ultra-sensitive all-fibre photothermal spectroscopy with large dynamic range. Nature Communications. 2015;**6**:6767

[19] Bykov DS, Schmidt OA, Euser TG, Russell PSJ. Flying particle sensors in hollow-core photonic crystal fibre. Nature Photonics. 2015;**9**:1-14

[20] Cubillas AM, et al. Photonic crystal fibres for chemical sensing and photochemistry. Chemical Society Reviews. 2013;**42**:8629-8648

[21] Wu C, et al. In-line microfluidic refractometer based on C-shaped fiber assisted photonic crystal fiber Sagnac interferometer. Optics Letters. 2013;**38**:3283-3286

[22] Wang J, et al. Fiber-optic anemometer based on Bragg grating inscribed in metal-filled microstructured optical Fiber. IEEE Xplore: Journal of Lightwave Technology. 2016;**34**: 4884-4889

[23] Sun B, et al. Microstructured-core photonic-crystal fiber for ultra-sensitive refractive index sensing. Optics Express. 2011;**19**:4091-4100

[24] Ebendorff-Heidepriem H, Warren-Smith S. Suspended nanowires: Fabrication, design and characterization of fibers with nanoscale cores. Optics Express. 2009;**17**:2646-2657

[25] Large MCJ, et al. Microstructured polymer optical fibres: New opportunities and challenges. Molecular Crystals and Liquid Crystals. 2006;**446**:219-231

[26] El-Amraoui M, et al. Microstructured chalcogenide optical fibers from As2S3 glass: Towards new IR broadband sources. Optics Express. 2010;**18**:26655-26665

[27] Tse M-LV, et al. Superlattice microstructured optical Fiber. Materials (Basel). 2014;**7**:4567-4573

[28] Chen D, Vincent Tse ML, Tam HY. Super-lattice structure photonic crystal fiber. Progress in Electromagnetics Research. 2010;**11**:53-64

[29] Fitt A, Furusawa K, Monro T. The mathematical modelling of capillary drawing for holey fibre manufacture. Journal of Engineering Mathematics. 2002;**43**:201-227

[30] Htein L, Liu Z, Tam HY. Hydrostatic pressure sensor based on fiber Bragg grating written in single-ring suspended fiber. Proc. SPIE 9916, Sixth Eur. Work. Opt. Fibre Sensors 99161R; 2016. DOI:10.1117/12.2235842

[31] Chen D, Hu G, Chen L. Dual-core photonic crystal Fiber for hydrostatic pressure sensing. IEEE Photonics Technology Letters. 2011;**23**:1851-1853

[32] Zhang L. Polarization-dependent coupling in twin-core photonic crystal fibers. Journal of Lightwave Technology. 2004;**22**:1367-1373

[33] Tse MLV, et al. Fusion splicing holey Fibers and single-mode Fibers: A simple method to reduce loss and increase strength. IEEE Photonics Technology Letters. 2009;**21**:164-166

[34] Xiao L, Jin W, Demokan MS. Fusion splicing small-core photonic crystal fibers and single-mode fibers by repeated arc discharges. Optics Letters. 2007;**32**:115-117

[35] Noda J, Okamoto K, Sasaki Y. Polarization-maintaining fibers and their applications. Journal of Lightwave Technology. 1986;**4**:1071-1089

[36] Zhu M, Murayama H, Wada D, Kageyama K. Dependence of measurement accuracy on the birefringence of PANDA fiber Bragg gratings in distributed simultaneous strain and temperature sensing. Optics Express. 2017;**25**:4000

[37] Dong X, Tam HY, Shum P. Temperature-insensitive strain sensor with polarization-maintaining photonic crystal fiber based Sagnac interferometer. Applied Physics Letters. 2007;**90**:151113

[38] Chen T, et al. Distributed high-temperature pressure sensing using air-hole microstructural fibers. Optics Letters. 2012;**37**(6):1064

[39] Weiguo C, et al. Highly sensitive torsion sensor based on Sagnac interferometer using side-leakage photonic crystal Fiber. IEEE Photonics Technology Letters. 2011;**23**:1639-1641

[40] Liu Z, Wu C, Tse M-LV, Lu C, Tam H-Y. Ultrahigh birefringence index-guiding photonic crystal fiber and its application for pressure and temperature discrimination. Optics Letters. 2013;**38**:1385-1387

[41] Suzuki K, Kubota H, Kawanishi S, Tanaka M, Fujita M. Optical properties of a low-loss polarization-maintaining photonic crystal fiber. Optics Express. 2001;**9**:676-680

[42] Edahiro T, Sasaki Y, Hosaka T, Miya T, Okamoto K. Low-loss single polarisation fibres with asymmetrical strain birefringence. Electronics Letters. 1981;**17**:530-531

[43] Birch RD, Payne DN, Varnham MP. Fabrication of polarisation- maintaining fibres using gas-phase etching. Electronics Letters. 1982;**18**:1036-1038

[44] Ortigosa-Blanch A, Knight J, Wadsworth W. Highly birefringent photonic crystal fibers. Optics Letters. 2000;**25**:1325-1327

[45] Frazão O, et al. Simultaneous measurement of multiparameters using a Sagnac interferometer with polarization maintaining side-hole fiber. Applied Optics. 2008;**47**:4841-4848

[46] Kim S, et al. Ultrahigh birefringence of elliptic core fibers with irregular air holes. Journal of Applied Physics. 2007;**102**:16101

[47] Martynkien T, et al. Highly birefringent microstructured fibers with enhanced sensitivity to hydrostatic pressure. Optics Express. 2010;**18**:15113-15121

[48] Beltrán-Mejía F, et al. Ultrahigh-birefringent squeezed lattice photonic crystal fiber with rotated elliptical air holes. Optics Letters. 2010;**35**:544-546

[49] Hansen TP, et al. Highly birefringent index-guiding photonic crystal fibers. IEEE Photonics Technology Letters. 2001;**13**:588-590

[50] Shi J, Feng X, Horak P, Poletti F. A fiberized highly birefringent glass micrometer-size ridge waveguide. Optical Fiber Technology. 2015;**23**:137-144

[51] Ortigosa-Blanch A. Ultrahigh birefringent nonlinear microstructured fiber. IEEE Photonics Technology Letters. 2004;**16**:1667-1669

[52] Chen X, et al. Highly birefringent hollow-core photonic bandgap fiber. Optics Express. 2004;**12**:3888-3893

[53] Pei T-H, Zhang Z, Zhang Y. The high-birefringence asymmetric SF57 glass microstructured optical fiber at 1060.0 um. Optical Fiber Technology. 2017;**36**:265-270

[54] Caillaud C, et al. Highly birefringent chalcogenide optical fiber for polarization-maintaining in the 3-8.5 μm mid-IR window. Optics Express. 2016;**24**:7977

[55] Hill KO, Meltz G. Fiber Bragg grating technology fundamentals and overview. Journal of Lightwave Technology. 1997;**15**:1263-1276

[56] Jewart CM, et al. Ultrafast femtosecond-laser-induced fiber Bragg gratings in air-hole microstructured fibers for high-temperature pressure sensing. Optics Letters. 2010;**35**: 1443-1445

[57] Groothoff N, Canning J, Buckley E, Lyttikainen K, Zagari J. Bragg gratings in air-silica structured fibers. Optics Letters. 2003;**28**:233-235

[58] Geernaert T, et al. Fiber Bragg gratings in germanium-doped highly birefringent microstructured optical fibers. IEEE Photonics Technology Letters. 2008;**20**:554-556

[59] Guan B, Chen D, Zhang Y. Bragg gratings in pure-silica polarization-maintaining photonic crystal fiber. IEEE Photonics Technology Letters. 2008;**20**:1980-1982

[60] Xu M, Reekie L, Chow Y, Dakin JP. Optical in-fibre grating high pressure sensor. Electronics Letters. 1993;**29**:398-399

[61] Wu C, Guan B-O, Wang Z, Feng X. Characterization of pressure response of Bragg gratings in grapefruit microstructured Fibers. Journal of Lightwave Technology. 2010;**28**: 1392-1397

[62] Liu Z, Tse MV, Zhang AP, Tam H. Integrated microfluidic flowmeter based on a micro-FBG inscribed in Co2+−doped optical fiber. Optics Letters. 2014;**39**:5877-5880

[63] Kersey AD. Optical fiber sensors for permanent downwell monitoring applications in the oil and gas industry. IEICE Transactions on Electronics. 2000;**83**:400-404

[64] Nakstad H, Kringlebotn JT. Oil and gas applications: Probing oil fields. Nature Photonics. 2008;**2**:147-149

[65] Anuszkiewicz A, et al. Sensing characteristics of the rocking filters in microstructured fibers optimized for hydrostatic pressure measurements. Optics Express. 2012;**20**:23320

[66] Kakarantzas G, et al. Structural rocking filters in highly birefringent photonic crystal fiber. Optics Letters. 2003;**28**:158-160

[67] Fu HY, et al. High pressure sensor based on photonic crystal fiber for downhole application. Applied Optics. 2010;**49**:2639-2643